Int J Adv Manuf Technol (2015) 79:1209–1219
DOI 10.1007/s00170-015-6895-7

ORIGINAL ARTICLE

Microscopic mechanism based force prediction in orthogonal cutting of unidirectional CFRP

Zhenchao Qi · Kaifu Zhang · Hui Cheng · Dong Wang · Qingxun Meng

Received: 30 September 2014 / Accepted: 9 February 2015 / Published online: 28 February 2015

Abstract The usage of carbon-fiber-reinforced polymer (CFRP) composite keeps increasing in modern industries. However, the machining mechanism of CFRP, especially the microscopic machining mechanism, is not well understood yet. This paper aims to establish a force prediction model for orthogonal cutting of unidirectional CFRP (UD-CFRP) in microscale. The deflection of the representative volume element (RVE), composed of a single fiber and the surrounding matrix, is analyzed considering the effect of the surrounding materials based on the minimum potential energy principle (MPEP). The critical force in the cutting edge that causes fracture of the RVE is obtained according to the bending deflection expression of the RVE. In addition, by taking slipping, peeling, and bounding mechanism in three different deformation areas into consideration, a force prediction model of UD-CFRP orthogonal cutting is established for fiber orientation ranging from 0° to γ_α+90°. Several experiments have been conducted, and the results comparison shows that the model, though approximately, has gotten acceptable agreement with the experimental results, which proves the effectiveness of the analysis method.

Keywords UD-CFRP · Microscopic mechanism · RVE · Orthogonal cutting · Force prediction model

1 Introduction

CFRP composite's usage in aviation, aerospace, and automotive industries has been steadily increasing due to its high specific strength, high specific modulus, high resistance to corrosion, and low thermal expansion coefficient [1]. In manufacturing and assembling process, an important aspect of production technology is machining, such as edge milling [2] and hole making [3]. In order to process CFRP better by machining, such as achieving high-precision surface without delamination, fiber pull-out, and burning, there is a need to develop a model of the machining of CFRP [4–8]. The major difficulty in modeling machining of CFRP is that the mechanism of the process is not completely understood. The machining mechanism of CFRP is different from that of conventional metals and alloys due to the anisotropic and heterogeneous nature of the materials [9]. However, in order to understand the machining mechanism of drilling or milling of CFRP, the analytical approach of orthogonal cutting [10] is worth considering. There are some research literatures focusing on the orthogonal cutting of CFRP. They aimed to obtain the regularity of the machining behavior and establish the predicting model of cutting forces.

Koplev et al. [11] examined the cutting of unidirectional CFRP using shaping experiments, quick-stop experiments, and a new chip preparation technique. They put forward the thesis for the first time that the formation of the chips is induced by the fracture of fiber and matrix. Wang et al. [12] and Albert et al. [13] did some experimental studies on machining of unidirectional composites, and they found that the material removal and chip formation were primarily dependent on fiber orientation. Işık [14] examined the surface roughness of unidirectional glass-fiber reinforced plastic composite on the basis of cutting parameters such as depth of cut, feed rate, tool geometry, and cutting speed. Next, Işık and Ekici [15] presented a new comprehensive approach to select cutting parameters for damage factor in drilling of glass-fiber-reinforced polymer (GFRP) composite material and investigated the influence of drilling on surface quality of woven GFRP plastic composite material experimentally. Subsequently, scholars made many attempts on the CFRP machining through finite element method (FEM), theoretical modeling method and

Z. Qi · K. Zhang (✉) · H. Cheng · Q. Meng
Northwestern Polytechnical University, Xi'an, Shaanxi, China
e-mail: zhangkf@nwpu.edu.cn

D. Wang
AVIC Xi'an Aircraft Industry (GROUP) Company LTD, Xi'an, Shaanxi, China

experimental method. Arola and Ramulu [16] used the FEM to simulate chip formation incorporating both the maximum stress and Tsai-Hill failure criteria. Their study is a good start for FEM of the CFRP machining, but they modeled the composite workpiece as an equivalent homogeneous material, which led to the limitation of the model in describing the fracture of fiber and matrix. Taking this into consideration, Rao et al. [17, 18] modeled the composite material as a multiphase material with cohesive zones as the interface between fibers and matrix material. They predicted the damage and chip formation mechanism for fiber orientation less than $\pi/2$ using ABAQUS/Standard FE code [17] and ABAQUS/Explicit FE code [18], respectively. All the prior FEM models that have been developed are quasi-static, and they are only capable of predicting the location of failure in the first fiber encountered by the tool rather than describing the failure mechanisms in forming a full chip. Chakladar et al. [19] estimated the drilling responses using finite element as a numerical simulation tool and established an equivalent elastic macromechanical model for the woven composite workpiece. A 3D drill bit was modeled using commercial CAD package Pro-Engineer and Ansys Autodyn was used as the solver environment. Calzada et al. [20] introduced a new approach to interfacial modeling using continuum elements allowing failure to take place in either tension or compression. The model was capable of describing the fiber failure mode occurring throughout the chip formation process.

The FEM models reveal some mechanism of CFRP machining and display the chip formation process visually. However, they do not explicitly uncover the mapping relationship between the cutting forces and key variables, such as fiber orientation, depth of cut, and fiber diameter. Furthermore, the FEM models are not suitable for machining process optimization, which usually needs a lot of iterations. So, as a result, mechanical force models established through theoretical analysis are of crucial importance. Bhatnagar et al. [21] did early attempts to predict forces in cutting unidirectional CFRP. They ascribed fiber breakage to axial tension as the cutting mechanism and finally presented a model for predicting the cutting forces using the shear plane theory. Zhang et al. [22–24] suggested that fiber microbuckling, fiber-matrix debonding, and fiber bending cause the machining forces and developed an approximate mechanical model to predict the forces in the orthogonal cutting of unidirectional CFRP when the fiber orientation varies from 0 to $\pi/2$. Their model was based on the shear plane theory and borrowed some idea from the metal cutting models. The direct consequence is that a few experiments need to be developed to obtain some of the parameters when using this model for a specific CFRP. Singh and Bhatnagar [25] made an effort to correlate drilling-induced damage with drilling parameters and proposed mathematical models for thrust, torque, and damage. Rahmé et al. [26] developed an orthotropic analytical model in order to calculate the critical force during drilling and proposed a number of hypotheses for loading. This critical axial load is related to the delamination conditions (propagation of cracks in the last layers) and the mechanical characteristics of the composite material machined. Sahraie Jahromi and Bahr [27] recognized that models based on shear plane theory have limitation in predicting the CFRP cutting forces. They developed a new analytical method using energy method to predict the orthogonal machining forces of unidirectional polymer matrix composites for fiber orientations ranging from $\pi/2$ to π. Their research is of great significance to prompt the representation of CFRP microstructure to transform from an equivalent homogeneous material to a multiphase material, just like the contribution Rao et al. [17, 18] did in the field of FEM. A RVE was taken out of the CFRP, and the pressure situation was analyzed. The complex interactions between the selected RVE and the other ones were simplified, which caused that the model needs to improve for more precise results of CFRP cutting force predicting.

Considering the support effect of the surrounding materials, the deflection differential equation is obtained by means of energy method and MPEP based on the assumption of semi-infinite RVE. Forces in three deformation areas relating to the cutting edge, the rake face and the flank face of the cutting tool were calculated separately. And finally, a new theoretical analysis model was developed to predict the orthogonal cutting forces of unidirectional CFRP with the fiber orientations ranging from 0° to γ_α+90° in this paper.

2 Analysis of orthogonal cutting

The deformation is different on the different load conditions when cutting the unidirectional CFRP with the fiber orientation θ limited into the range 0° to 90° and 90° to 180° (the list of symbols used is shown in Table 1) [22]. Taking the rake angle in orthogonal cutting tool γ_α into consideration, a more accurate classification is limited θ into the range $0°\le\theta\le\gamma_\alpha+90°$ and $\gamma_\alpha+90°\le\theta\le180°$. This study will focus on analyzing the mechanism of unidirectional CFRP cutting when $0°\le\theta\le\gamma_\alpha+90°$, as shown in Fig. 1. The modeling with $\gamma_\alpha+90°\le\theta\le180°$ will be discussed in a separate paper.

The CFRP machining region associated with the cutting forces could be divided into three major areas, marked as *A*, *B*, and *C* as shown in Fig. 1. It is an instantaneous state at a certain moment when the cutting edge cuts off RVE 1 and RVE 2, while the damage of RVE 3 just has not begun. The cutted RVEs, RVE 1' and RVE 2', slip along the rake face in cutting edge, and form the cutting chip. In area *A*, the fracture of the fiber occurs due to the compression and bending. In area *B*, the RVEs are compressed by the flank face of the cutting edge and they bounce back as the cutting edge moving forward. The matrix failure and fiber matrix debonding exist in

Table 1 Nomenclature

A_m	Area of the cross section of matrix	a_c	Cutting depth
E_b	Equivalent young' s modulus of the RVE	b	Cutting width
E_f	Young's modulus of the fiber	f_A	Friction produced by F_U
E_m	Young's modulus of the matrix	h_c	Indentation depth
E_D	Young's modulus of the bounding area	k	Coefficient of cushion
F_A	Resultant force in area A	p_b	Distributed force produced by the other RVEs
F_C	Resultant force in area C	r_f	Fiber radius
F_D	Resultant force in area D	r_m	Radius of the RVE
F_U	Normal concentrated force applied by the cutting edge	r_t	Cutting edge radius
G_m	Shear modulus of the matrix	γ_α	Rake angle in cutting edge
H	Cushion thickness	γ_β	Relief angle in cutting edge
I_f	Second moment of area of the cross section of the fiber	γ_{yzm}	Shear strain in the matrix material in the yz plane
L_c	Distance between the fiber free end and the origin of the local coordinate system O	η	Distance of an arbitrary point to the neutral layer
M	Bending moment	θ	Fiber orientation
Q	Shearing force	μ	Friction coefficient
S_m	Matrix shear strength	ν_f	Poisson ratio of the fiber
U_f	Elastic strain energy of the fiber	φ	Angle of rotation
U_m	Shear strain energy in the matrix	ω	Central axis deflection of the RVE
W_{FU}	Work of the external force	ψ	Angle between the rake face and the fiber
W_{Pb}	Work of the external pressure	Φ	Shear plane angle
X_f	Fiber ultimate strength	α, β, m	Middle variable to simplify the writing
vol_f	Fiber volume fraction	c_1, c_2, c_3, c_4, c_5, c_6	Correlation coefficients

area C. All these areas contribute to the final cutting force, but the fiber fragmentation plays a most important role. Therefore, the key to develop the force predicting model is taking RVE 3 out and analyzing it in reasonable load condition.

3 Mechanical analysis of RVE 3

3.1 Deflection function of RVE 3

RVE 3, consisted of a fiber and the surrounding matrix, bends under the force F_U and passive pressure p_b, as shown in Fig. 2.

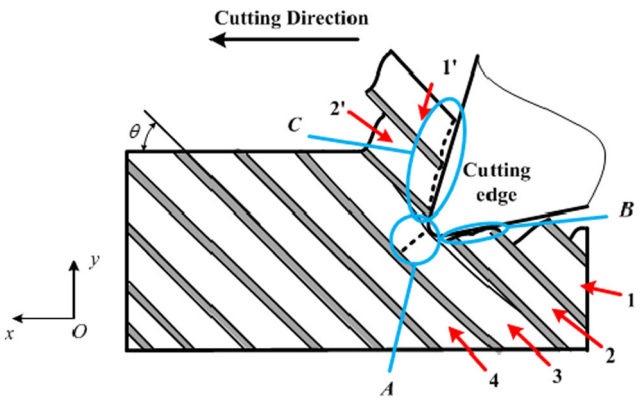

Fig. 1 Orthogonal cutting of unidirectional CFRP when $0°\leq\theta\leq\gamma_\alpha+90°$

Since the length of the contact area is far smaller than the length of the deformed fiber, the load applied on the contact area by the cutting edge could be regarded as a concentrated force, denoted by F_U. p_b is a distributed force produced by the other RVEs, and its distribution law depends on the deflection of RVE 3. Making convenience of analysis and computation, a local coordinate system is set up based on the origin O, which

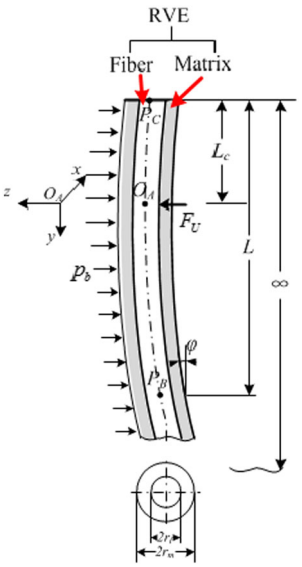

Fig. 2 Load condition of RVE 3

is in the central axis of the fiber related with the contact point of the RVE and cutting edge, as shown in Fig. 2.

Before the analysis, some assumptions are proposed on the basis of former studies [27, 28].

1. Two-dimensional deformation
2. No shear in the fiber
3. No matrix extension or compression
4. Normal stress in the fiber that produces no mechanical work during deformation of the fiber

The stress state of the key point could be calculated based on the deflection of the RVE. To obtain the deflection equation, energy method and MPEP are used based on the assumption of semi-infinite RVE.

Since the fiber satisfied the condition of slender beam, the elastic strain energy of the fiber could be expressed as [29]

$$U_f = \frac{1}{2}\int_{-L_c}^{\infty} E_f I_f \left(\frac{d^2\omega}{dy^2}\right)^2 dy \tag{1}$$

So, the shear strain energy of the matrix will be

$$\begin{aligned} U_m &= \frac{1}{2}\int_{-L_c}^{\infty} G_m \gamma_{yzm}^2 A_m dy \\ &= \frac{1}{2} A_m G_m \left(\frac{r_m}{r_f}\right)^2 \int_{-L_c}^{\infty} \left(\frac{d\omega}{dy}\right)^2 dy \end{aligned} \tag{2}$$

where

$$A_m = \frac{\pi {r_f}^2 (1 - vol_f)}{vol_f} \tag{3}$$

and

$$r_m = \frac{1}{2}\sqrt{\frac{\pi}{vol_f}} r_f \tag{4}$$

The work of the external force F_U could be written as

$$W_{F_U} = F_U \omega\big|_{y=0} \tag{5}$$

Using the Winkler foundation model [30] as reference, the passive pressure p_b could be represented as

$$dp_b(y) = -\frac{E_b}{H}\omega(y)\cdot 2 r_m dy \tag{6}$$

where E_b is the equivalent Young's modulus associating with E_f and E_m. The supporting function of the uncut fiber and matrix is similar to the cascade spring connection, so E_b could be expressed as

$$E_b = \frac{E_f E_m}{E_f + E_m} \tag{7}$$

For convenient calculation, a dimensionless coefficient k is introduced to modify the cushion thickness H.

$$H = 2 k r_m \tag{8}$$

Substituting Eqs. (8) into (6), we get

$$dp_b(y) = -\frac{E_b dy}{k}\omega(y) \tag{9}$$

The work of the external pressure p_b could be expressed as

$$W_{p_b} = \int_{-L_c}^{\infty} \omega dp_b = -\frac{E_b}{k}\int_{-L_c}^{\infty} \omega^2 dy \tag{10}$$

Combining Eqs. (1), (2), (5), and (10), the total potential energy of RVE 3 will be

$$\begin{aligned} \Pi &= U_f + U_m - W_{F_U} - W_{p_b} \\ &= \frac{1}{2}\int_{-L_c}^{\infty} E_f I_f \left(\frac{d^2\omega}{dy^2}\right)^2 dy \\ &\quad + \frac{1}{2} A_m G_m \left(\frac{r_m}{r_f}\right)^2 \int_{-L_c}^{\infty} \left(\frac{d\omega}{dy}\right)^2 dy - F_U \omega\big|_{y=0} \\ &\quad + \frac{E_b}{k}\int_{-L_c}^{\infty} \omega^2 dy \end{aligned} \tag{11}$$

According to the MPEP, the unite cell deforms to a final position that minimize the total potential energy. The first order variational of the functional equals to zero, namely $\delta\Pi = 0$. Then, the following equation could be obtained as

$$E_f I_f \left(\omega^{(4)}\right) - A_m G_m \left(\frac{r_m}{r_f}\right)^2 \omega'' + \frac{2E_b}{k}\omega = 0 \tag{12}$$

Considering the assumption of semi-infinite RVE, the general solution of the differential Eq. (12) is

$$\omega(y) = c_1 e^{-\alpha y}\cdot\cos\beta y + c_2 e^{-\alpha y}\cdot\sin\beta y \tag{13}$$

where

$$\alpha = \frac{\sqrt[4]{A_m {G_m}^2 + m^2}\cos\left(\frac{1}{2}\arctan\frac{m}{A_m G_m}\right)}{\sqrt{2E_f I_f}} \tag{14}$$

$$\beta = \frac{\sqrt[4]{A_m G_m{}^2 + m^2}\sin\left(\frac{1}{2}\arctan\frac{m}{A_m G_m}\right)}{\sqrt{2E_f I_f}} \tag{15}$$

$$m = \sqrt{(A_m G_m)^2\left(\frac{r_m}{r_f}\right)^4 - 4E_f I_f \frac{2E_b}{k}} \tag{16}$$

The deflection equation of the unite cell could be obtained in two steps. The first step is to extend the free end of the RVE limitlessly, and then, the RVE turns to be infinite, shown in Fig. 3b. Since the RVE is symmetrical with point O_A as the center, the deflection equation should be symmetrical as well. Considering the direction of increasing y, the boundary conditions of point O_A could be calculated by

$$\phi = \omega'(y) = 0 \tag{17}$$

$$Q = -E_f I_f \omega'''(y) = -\frac{F_U}{2} \tag{18}$$

Solve Eqs. (17) and (18) simultaneously, and then the correlation coefficients are obtained as

$$c_1 = \frac{F_U}{4E_f I_f \alpha(\alpha^2 + \beta^2)} \tag{19}$$

$$c_2 = \frac{F_U}{4E_f I_f \beta(\alpha^2 + \beta^2)} \tag{20}$$

Because of the symmetry of the RVE, the deflection function of the infinite RVE could be written as

$$\omega_a(y) = c_1 e^{-\alpha|y|}\cdot\cos\beta|y| + c_2 e^{-\alpha|y|}\cdot\sin\beta|y| \tag{21}$$

In the model of infinite RVE shown in Fig. 3b, the bending moment and shearing force of the cross section at point P_C may be described as

$$M_0 = -E_f I_f \omega_a''\big|_{y=-L_c} \tag{22}$$

$$Q_0 = -E_f I_f \omega_a'''\big|_{y=-L_c} \tag{23}$$

The infinite RVE would turn to be semi-infinite when it was cut off at cross section at point P_C. Compared with the real state of the RVE shown in Fig. 3a, this semi-infinite model bears extra load M_0 and Q_0. Therefore, the second step is to remove the extra load.

As shown in Fig. 3c, two load, $-M_0$ and $-Q_0$, are applied on the free end of a semi-infinite RVE. The general form of the deflection function could be expressed as

$$\omega_b(y) = c_5 e^{-\alpha y}\cdot\cos\beta y + c_6 e^{-\alpha y}\cdot\sin\beta y \tag{24}$$

The boundary conditions of the free end will be written as

$$-E_f I_f \omega_b''\big|_{y=-L_c} = -M_0 \tag{25}$$

$$-E_f I_f \omega_b'''\big|_{y=-L_c} = -Q_0 \tag{26}$$

Solve Eqs. (25) and (26) simultaneously, and then, the correlation coefficients c_5 and c_6 could be obtained. Substituting c_5 and c_6 into Eq. (24), and combining

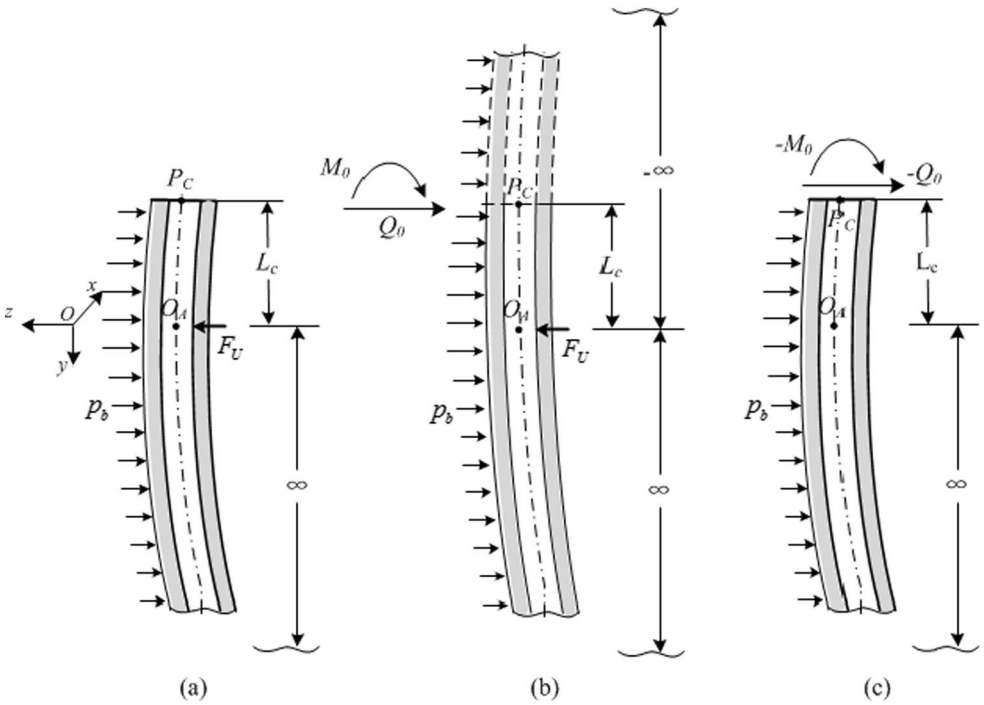

Fig. 3 Solving process of the deflection equation

with Eq. (21), the final deflection function of RVE in Fig. 3a could be obtained as

$$\omega(y) = c_1 e^{-\alpha|y|}\cdot\cos\beta|y| + c_2 e^{-\alpha|y|}\cdot\sin\beta|y| + c_5 e^{-\alpha y}\cdot\cos\beta y + c_6 e^{-\alpha y}\cdot\sin\beta y \quad (27)$$

3.2 Force determination by ultimate strength

The relationship of the normal concentrated force F_u and the deflection ω is obtained in the last section. And, in this section, the force F_u would be determined by introducing the relationship of ω and the fiber ultimate strength X_f.

The stress caused by the deformation of the RVE could be calculated by [31]

$$\sigma_{\bar{y}} = E_f \eta \omega'' \quad (28)$$

where η is the distance of an arbitrary point to the neutral layer. It would be a positive value when the point locates on the left of the neutral layer and a negative one when the point locates on the right.

When η equals to r_f and $-r_f$, the absolute value of the deformation stresses reach to the maximum value. Since the compressive strength of fiber is larger than the tensile strength, the fracture of the fiber starts at the point where η equals to r_f. The normal concentrated force F_U applied by the cutting edge could be determined by

$$E_f r_f \omega''\big|_{y=0} = X_f \quad (29)$$

Then, we get

$$F_U = \frac{4\alpha\beta I_f X_f e^{2\alpha L_c}}{r_f[\beta e^{2\alpha L_c} - \beta\cos(2\beta L_c) + \alpha\sin(2\beta L_c)]} \quad (30)$$

where α and β are determined by Eqs. (14), (15), and (16).

4 Force modeling of orthogonal cutting

The cutting force when machining the unidirectional CFRP is a superimposition of the forces in fiber fracturing, bouncing, and chip slipping regions, which occur in area A, area B, and area C, respectively, as shown in Fig. 1. It is worth mentioning that the fiber matrix debonding in area B occurs prior to the fiber fracturing; thus, the debonding force makes no contribution to the maximum instantaneous cutting force.

The loading condition of area A is shown in Fig. 4. The friction produced by the normal concentrated force applied by the cutting edge is given by

$$f_A = \mu F_U = \frac{4\mu\alpha\beta I_f X_f e^{2\alpha L_c}}{r_f[\beta e^{2\alpha L_c} - \beta\cos(2\beta L_c) + \alpha\sin(2\beta L_c)]} \quad (31)$$

where

$$L_c = \frac{a_c}{\sin\theta} \quad (32)$$

The horizontal force and the vertical force of area A could be written as

$$\begin{cases} F_{Ax} = F_U\sin\theta + f_A\cos\theta = \dfrac{4\alpha\beta I_f X_f e^{2\alpha L_c}}{r_f[\beta e^{2\alpha L_c} - \beta\cos(2\beta L_c) + \alpha\sin(2\beta L_c)]}(\mu\cos\theta + \sin\theta) \\ F_{Ay} = -F_U\cos\theta + f_A\sin\theta = \dfrac{4\alpha\beta I_f X_f e^{2\alpha L_c}}{r_f[\beta e^{2\alpha L_c} - \beta\cos(2\beta L_c) + \alpha\sin(2\beta L_c)]}(\mu\sin\theta - \cos\theta) \end{cases} \quad (33)$$

The loading condition of area C is shown in Fig. 5. According to the geometrical relationship, we get

$$\psi = \frac{\pi}{2} - \theta + \gamma_\alpha \quad (34)$$

When $\psi \geq 90°$, namely $\theta \geq \gamma_\alpha$, the chips formed by the fractured RVEs slip along the uncut RVE, which causes the matrix shear failure, as shown in Fig. 5a. The force associated with the matrix shear failure could be estimated by

$$F_S = 2r_m L_C S_m = \frac{2r_m a_C S_m}{\sin\theta} \quad (35)$$

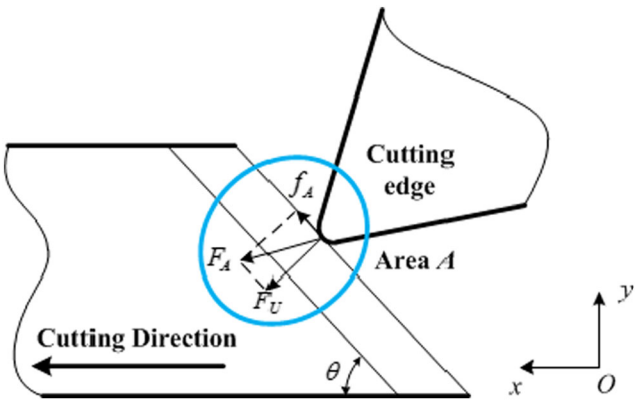

Fig. 4 Loading condition of area A

The total force is

$$F_{C1} = \frac{F_S}{\cos(\varphi - \gamma_\alpha + \arctan\mu)} = \frac{2r_m a_C S_m}{\sin\theta\cos(\varphi - \gamma_\alpha + \arctan\mu)} \tag{36}$$

where ϕ is the shear plane angle determined by [22]

$$\varphi = \arctan\left(\frac{\cos\gamma_\alpha}{1-\sin\gamma_\alpha}\right) \tag{37}$$

The horizontal component force and the vertical component force are

$$\begin{cases} F_{Cx} = F_{C1}\cos(\gamma_\alpha - \arctan\mu) = \dfrac{2r_m a_C S_m(\sin\gamma_\alpha + \mu\cos\gamma_\alpha)\cos(\gamma_\alpha - \arctan\mu)}{\sin\theta\cos(\varphi - \gamma_\alpha + \arctan\mu)} \\ F_{Cy} = F_{C1}\sin(\gamma_\alpha - \arctan\mu) = \dfrac{2r_m a_C S_m(\sin\gamma_\alpha + \mu\cos\gamma_\alpha)\sin(\gamma_\alpha - \arctan\mu)}{\sin\theta\cos(\varphi - \gamma_\alpha + \arctan\mu)} \end{cases} \tag{38}$$

When $\psi<90°$, namely $\theta<\gamma_\alpha$, the RVEs are pelt off due to the force produced by the rake face, as shown in Fig. 5b. The force could be expressed by [32]

$$F_{C2} = K_P\sqrt{\frac{2(1-\nu_{EHM})G_m}{E_{EHM}}}\pi\frac{a_c}{\cos\theta}S_m\cot\gamma_\alpha \tag{39}$$

The demarcation point of the separate function is $\theta=\gamma_\alpha$, so we get

$$\frac{2K_S r_m a_C S_m}{\sin\gamma_\alpha\cos(\varphi - \gamma_\alpha + \arctan\mu)} = K_P\sqrt{\frac{2(1-\nu_{EHM})G_m}{E_{EHM}}}\pi a_c S_m\frac{\cot\gamma_\alpha}{\cos\gamma_\alpha} \tag{40}$$

Combining Eqs. (39) and (40),we get

$$F_{C2} = 2r_m a_C S_m\frac{\cot\gamma_\alpha}{\cos(\varphi - \gamma_\alpha + \arctan\mu)\cos\theta} \tag{41}$$

The total force in area C could be written as

$$F_C = \begin{cases} \dfrac{2r_m a_C S_m\cot\gamma_\alpha}{\cos(\varphi - \gamma_\alpha + \arctan\mu)\cos\theta} & \theta < \gamma_\alpha \\ \dfrac{2r_m a_C S_m}{\sin\theta\cos(\varphi - \gamma_\alpha + \arctan\mu)} & \theta \geq \gamma_\alpha \end{cases} \tag{42}$$

The horizontal component force and the vertical component force are

$$\begin{cases} F_{Cx} = F_C\cos(\gamma_\alpha - \arctan\mu) \\ F_{Cy} = F_C\sin(\gamma_\alpha - \arctan\mu) \end{cases} \tag{43}$$

In area B, the contact force between the flank face and the workpiece material is caused by the bouncing back of the workpiece material. The horizontal force and the vertical force are [22, 33]

$$\begin{cases} F_{Bx} = r_m r_t E_B\cos^2\gamma_\beta \\ F_{By} = r_m r_t E_B(1 - \mu\cos\gamma_\beta\sin\gamma_\beta) \end{cases} \tag{44}$$

The models above are discussed with regard to the orthogonal cutting of a single layer of the RVE; in other words, the cutting width is $2r_m$. The total cutting force applied on the workpiece by the cutting edge is a superimposition of the forces in the three areas. Considering the orthogonal cutting of CFRP with an arbitrary cutting width b, the cutting force F_x and thrust force F_y could be expressed as

$$\begin{cases} F_x = \dfrac{b}{2r_m}(F_{Ax} + F_{Cx} + F_{Bx}) \\ F_y = \dfrac{b}{2r_m}(F_{Ay} + F_{Cy} + F_{By}) \end{cases} \tag{45}$$

5 Experimental setup

A series of experiments were performed to measure the cutting and thrust forces. Figure 6 shows the schematic view of the experimental setup. The experiments were carried on a XKN713 numerical control machining center. A cutting tool with specified geometric parameters was installed on the machine tool and moved along the x-coordinate axis. The

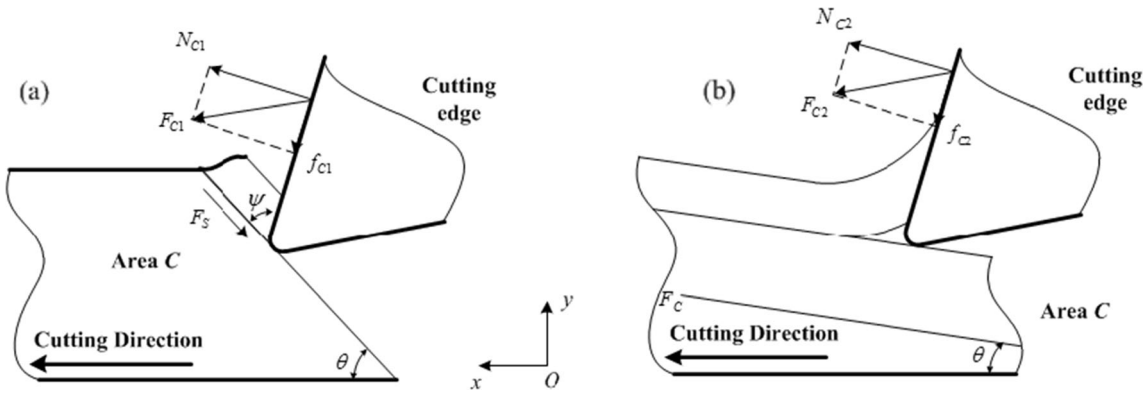

Fig. 5 **a** Loading condition of area C when $\theta\geq\gamma_\alpha$; **b** loading condition of area C when $\theta<\gamma_\alpha$

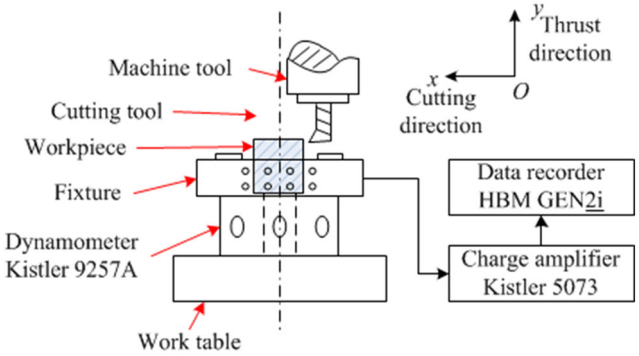

Fig. 6 Schematic of the experimental setup

workpiece with specified fiber orientation was fixed to the fixture which is mounted on the dynamometer. The cutting and thrust forces were measured by a Kistler 9257A quartz three-component platform dynamometer and Kistler 5073 charge amplifier, and recorded by a HBM GEN2i data recorder (Fig. 7).

Cemented carbide cutting tools with r_t=4 μm and γ_β=25° were used in the experiment. They were specially designed for orthogonal cutting with different rake angles γ_α=10° and γ_α=20°. UD-CFRP workpieces with the stacking sequences $[0°]_{15S}$ were designed for the experiment. The thickness per layer is 0.25 mm, and then, the total thickness is 3.75 mm. The material properties are given in Table 2.

Experiments with different fiber orientations (θ=0°, 30°, 45°, 60°, 90°), rake angle (γ_α=10°, 20°) and cutting depth (a_c=0.1 mm, 0.2 mm) were conducted. Each experiment with a special parameter combination was repeated three times. The cutting speed was kept 1 m/min for all the experiments. The friction coefficient between the fiber and the cutting edge was 0.15 in this situation. A sample of the measured cutting and thrust forces with θ=60°, γ_α=10°, and a_c=0.1 mm was shown in Fig. 8.

The experimental real-time force signals fluctuate up and down. As time goes on, the fluctuation stabilizes in a certain range gradually. The mathematical expectation of the forces in steady state were calculated and recorded as the experimental forces in cutting and thrust directions, respectively.

Table 2 List of material properties T700/5250BMI

Fiber radius (r_f)	3.5 μm	Young's modulus of the matrix (E_m)	2.7 GPa
Young's modulus of the fiber (E_f)	230 GPa	Shear modulus of the matrix (G_m)	1.02 GPa
Poisson ratio of the fiber (ν_f)	0.21	Fiber volume fraction (vol_f)	0.65
Fiber ultimate strength (X_f)	4.9 GPa	Poisson ratio of the matrix (ν_m)	0.33
Matrix shear strength (S_m)	62 MPa	Young's modulus of the bounding area (E_D)	9.4 GPa

6 Numerical illustration and result comparison

There is one coefficient, namely the coefficient of cushion k, in the theoretical force model to be determined by the experimental data. The experimental cutting forces with θ=45°, γ_α=10°, and a_c=0.1 mm were chosen, and the average of the repeated experimental data was 491.1 N. Then, the coefficient of cushion k was calibrated as 4.7E−4. The coefficient was taken into the theoretical model to predict the forces with different parameters. The comparisons of the theoretical and experimental results are shown in Fig. 9.

As can be seen, the fiber orientation has a significant effect on the forces. As shown in Fig. 9b, d, the cutting force increases and then decreases with the increase of the fiber orientation; meanwhile, the thrust force decreases and changed the direction when fiber orientation comes to 90°.

The cutting forces increase with the cutting depth, which phenomenon is more pronounced when the fiber orientation θ is kept as a smaller value. This is because the force produced

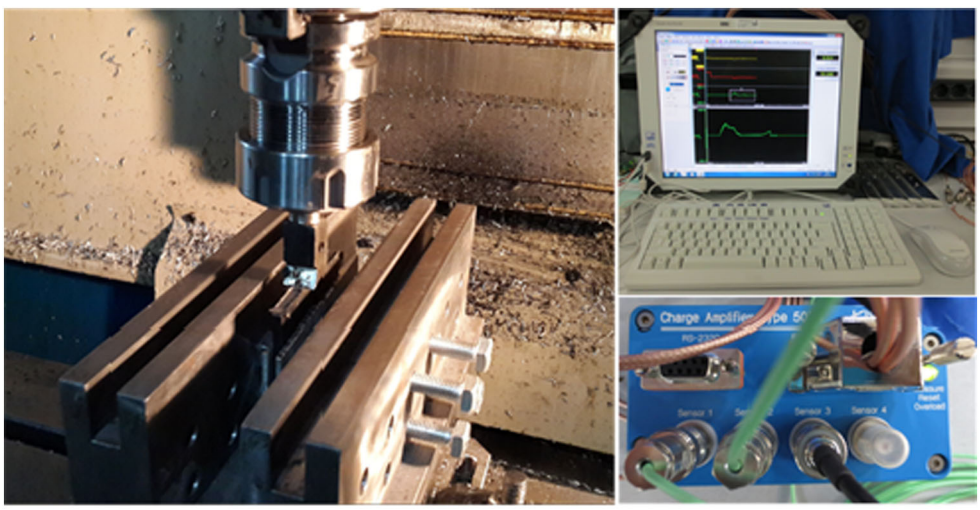

Fig. 7 Experimental setup

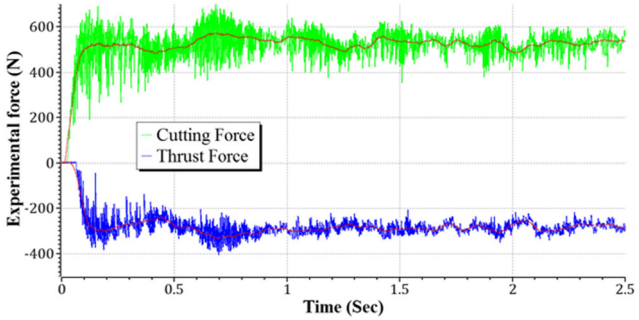

Fig. 8 Experimental cutting and thrust forces with θ=60°, γ_α=10°, and a_c=0.1 mm

by the rank edge plays a dominant role under this condition, and the effect of the cutting edge becomes more and more obvious as the fiber orientation increases.

A sharp point exists in the theoretical curve as shown in Fig. 9a, c. It is a result of different cutting mechanisms when $\theta < \gamma_\alpha$ and $\theta \geq \gamma_\alpha$, as shown in Fig. 5.

When the fiber orientation θ equals to 0° and 90°, the error of the theoretical model is more lager than the other fiber orientation value. When θ=0°, the RVEs are pelt off form the workpiece, bend more and more markedly, until they break and form the chips. When θ=90°, the crushing action of the rank face is too significant to ignore. It is the reason that the model is not accurate for all fiber orientations.

In addition, the cutting force is predicted in 2D condition, which means that the fibers behind the bending one is taken into consideration, but the ones on the sides are ignored; in other words, the interaction between the plies is ignored. The total force of multiplies is obtained by simple superposition. In fact, the interlaminar damage would lead to energy loss, which results in imprecise estimate of the cutting force. This might be another reason why the model is not accurate for all fiber orientations, especially when θ=0°.

Sahraie Jahromi and Bahr's model predicted the cutting forces for fiber orientations ranging from 90° to 180° [27]. The model presented in this paper is a developed one, considering the effect of the surrounding materials for fiber orientations ranging from 0° to γ_α+90°. The two models are complementary with only partial overlap, namely when fiber orientations ranging from 90° to γ_α+90°. It can be seen that the developed model has a better continuity than the previous one when comparing results in the overlap part. Zhang's model deals with fiber orientations ranging from 0° to 90° [22], and the tendency of the curve is close to the developed model. However, the thrust force predicted by the developed model is smaller than Zhang's model when θ=90°. This is because of different treatments of the force on the rake face. This model takes the RVE sliding and bending into consideration, which is more reasonable than the previous equivalent homogeneous models. The chips produce lager counterforce along $-y$ direction than the previous model. As a result, the resultant thrust force along y direction is smaller.

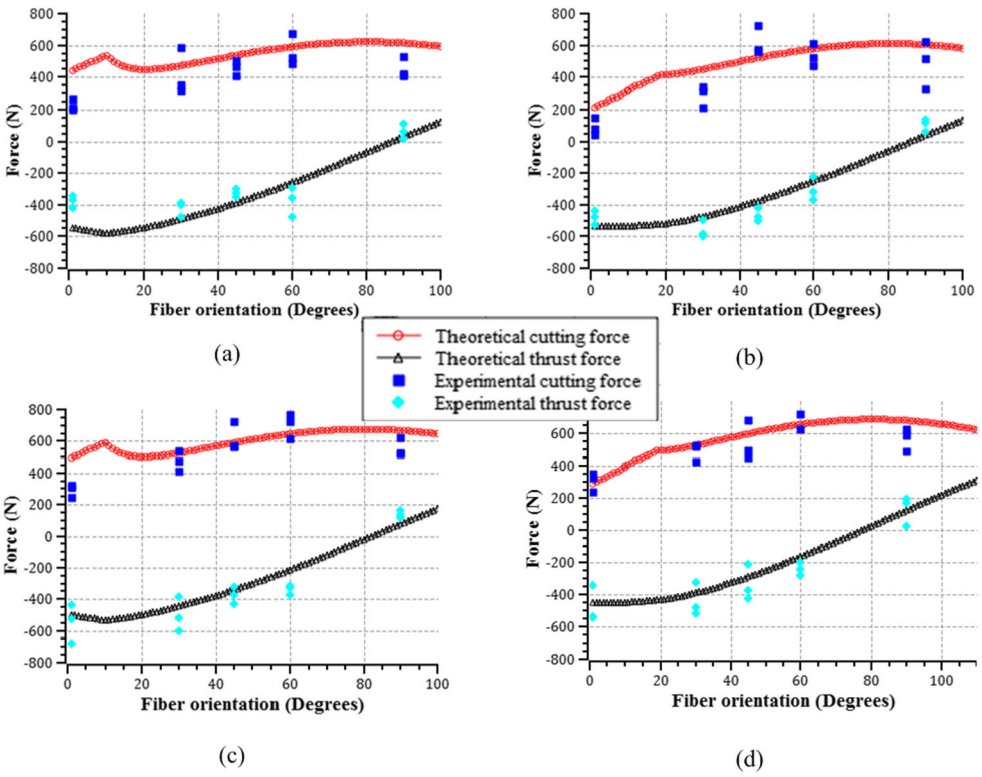

Fig. 9 Theoretical and experimental cutting and thrust forces versus fiber orientation with: (**a**) γ_α=10° and a_c=0.1 mm; (**b**) γ_α=20° and a_c=0.1 mm; (**c**) γ_α=10° and a_c=0.2 mm; and (**d**) γ_α=20° and a_c=0.2 mm

7 Conclusion

The paper develops a theoretical model for predicting the cutting and thrust forces in orthogonal cutting of UD-CFRP when $0°\leq\theta\leq\gamma_\alpha+90°$. Three deformation areas related to the cutting tool, fiber crushing, and bending caused by the cutting edge (area *A*), bouncing back under the flank face (area *B*), peeling and slipping on the rake face (area *C*), are taken into consideration. Fiber bending in area *A* is a key consideration and a predicting model is established based on the MPEP. The theoretical model shows that the fiber orientation, cutting depth, and rake angle have significant effects on the cutting and thrust forces.

This model could be used to predict the forces in machining of multidirectional CFRP, such as drilling, milling, and turning. It will make the parameter optimizing more convenient since the relationship of the material and cutting tool parameters to the cutting forces was established.

The actual force is a complex combination of various component forces according to different mechanism such as bending, crushing, shearing, microbuckling, peeling, and slipping. The effects of different mechanism keep changing, some of them strengthening while others lessening, as the fiber orientation increases. In this theoretical model, some mechanism is ignored for simplicity, which results in errors and calls for more following work for complement.

Acknowledgments The work reported herein is sponsored by the National Natural Science Foundation of China (51305352), Fund of national Engineering and Research Center for Commercial Aircraft Manufacturing, China (SAMC13-JS-15-029), "High-end NC Machine Tools and Basic Manufacturing Equipment," China (2014ZX04001-081), and "the Fundamental Research Funds for the Central Universities," China (3102014JCS05008). The authors would like to acknowledge the editors and the anonymous referees for their insightful comments.

References

1. Iliescu D, Gehin D, Iordanoff I, Girot F, Gutiérrez ME (2010) A discrete element method for the simulation of CFRP cutting. Compos Sci Technol 70(1):73–80
2. Chibane H, Morandeau A, Serra R, Bouchou A, Leroy R (2013) Optimal milling conditions for carbon/epoxy composite material using damage and vibration analysis. Int J Adv Manuf Technol 68(5–8):1111–1121
3. Silva D, Teixeira JP, Machado CM (2014) Methodology analysis for evaluation of drilling-induced damage in composites. Int J Adv Manuf Technol 71(9–12):1919–1928
4. Jayabal S, Natarajan U (2010) Optimization of thrust force, torque, and tool wear in drilling of coir fiber-reinforced composites using Nelder–Mead and genetic algorithm methods. Int J Adv Manuf Technol 51(1–4):371–381
5. Che D, Saxena I, Han P, Guo P, Ehmann KF (2014) Machining of carbon fiber reinforced plastics/polymers: a literature review. J Manuf Sci Eng 136(3):034001
6. Karpat Y, Deger B, Bahtiyar O (2014) Experimental evaluation of polycrystalline diamond tool geometries while drilling carbon fiber-reinforced plastics. Int J Adv Manuf Technol 71(5–8):1295–1307
7. Montoya M, Calamaz M, Gehin D, Girot F (2013) Evaluation of the performance of coated and uncoated carbide tools in drilling thick CFRP/aluminium alloy stacks. Int J Adv Manuf Technol 68(9–12): 2111–2120
8. Ben Soussia A, Mkaddem A, El Mansori M (2014) Rigorous treatment of dry cutting of FRP-Interface consumption concept: a review. Int J Mech Sci 83:1–29
9. Rahamathullah I, Shunmugam M (2014) Mechanistic approach for prediction of forces in micro-drilling of plain and glass-reinforced epoxy sheets. Int J Adv Manuf Technol 75(5–8):1177–1187
10. Zhou L, Hou N, Huang S, Xu L (2014) An experimental study on formation mechanisms of edge defects in orthogonal cutting of SiCp/Al composites. Int J Adv Manuf Technol 1–8
11. Koplev A, Lystrup A, Vorm T (1983) The cutting process, chips, and cutting forces in machining CFRP. Composites 14(4):371–376
12. Wang DH, Ramulu M, Arola D (1995) Orthogonal cutting mechanisms of graphite/epoxy composite. Part I: unidirectional laminate. Int J Mach Tools Manuf 35(12):1623–1638
13. Albert G, Laheurte R, K'Nevez J-Y, Darnis P, Cahuc O (2011) Experimental milling moment model in orthogonal cutting condition: to an accurate energy balance. Int J Adv Manuf Technol 55(9–12): 843–854
14. Işık B (2008) Experimental investigations of surface roughness in orthogonal turning of unidirectional glass-fiber reinforced plastic composites. Int J Adv Manuf Technol 37(1–2):42–48
15. Işık B, Ekici E (2010) Experimental investigations of damage analysis in drilling of woven glass fiber-reinforced plastic composites. Int J Adv Manuf Technol 49(9–12):861–869
16. Arola D, Ramulu M (1997) Orthogonal cutting of fiber-reinforced composites: a finite element analysis. Int J Mech Sci 39(5):597–613
17. Rao GVG, Mahajan P, Bhatnagar N (2007) Micro-mechanical modeling of machining of FRP composites-Cutting force analysis. Compos Sci Technol 67(3–4):579–593
18. Rao GVG, Mahajan P, Bhatnagar N (2007) Machining of UD-GFRP composites chip formation mechanism. Compos Sci Technol 67(11–12):2271–2281
19. Chakladar ND, Pal SK, Mandal P (2012) Drilling of woven glass fiber-reinforced plastic—an experimental and finite element study. Int J Adv Manuf Technol 58(1–4):267–278
20. Calzada KA, Kapoor SG, DeVor RE, Samuel J, Srivastava AK (2012) Modeling and interpretation of fiber orientation-based failure mechanisms in machining of carbon fiber-reinforced polymer composites. J Manuf Process 14(2):141–149
21. Bhatnagar N, Ramakrishnan N, Naik NK, Komanduri R (1995) On the machining of fiber reinforced plastic (FRP) composite laminates. Int J Mach Tools Manuf 35(5):701–716
22. Zhang LC, Zhang HJ, Wang XM (2001) A force prediction model for cutting unidirectional fibre-reinforced plastics. Mach Sci Technol 5(3):293–305
23. Wang XM, Zhang LC (2003) An experimental investigation into the orthogonal cutting of unidirectional fibre reinforced plastics. Int J Mach Tools Manuf 43(10):1015–1022
24. Zhang LC (2009) Cutting composites: A discussion on mechanics modelling. J Mater Process Technol 209(9):4548–4552
25. Singh I, Bhatnagar N (2006) Drilling of uni-directional glass fiber reinforced plastic (UD-GFRP) composite laminates. Int J Adv Manuf Technol 27(9–10):870–876
26. Rahmé P, Landon Y, Lachaud F, Piquet R, Lagarrigue P (2011) Analytical models of composite material drilling. Int J Adv Manuf Technol 52(5–8):609–617

27. Sahraie Jahromi A, Bahr B (2010) An analytical method for predicting cutting forces in orthogonal machining of unidirectional composites. Compos Sci Technol 70(16):2290–2297
28. Reifsnider KL (2002) Case SW. Damage tolerance and durability of material systems. John Wiley, New York
29. Beer F, Johnston E, DeWolf J (2002) Mechanics of Materials, 2002. McGraw-Hill, New York
30. Winkler E (1867) Theory of elasticity and strength. Prague, Dominicus
31. Boresi AP, Schmidt RJ, Sidebottom OM (1993) Advanced mechanics of materials. Wiley, New York
32. Everstine GC, Rogers TG (1971) A theory of machining of fiber-reinforced materials. J Compos Mater 5(1):94–106
33. Guo DM, Wen Q, Gao H, Bao YJ (2011) Prediction of the cutting forces generated in the drilling of carbon-fibre-reinforced plastic composites using a twist drill. P I Mech Eng B-J Eng 226(1):28–42